A Geometric Street Scattering Channel Model for Car-to-Car Communication Systems

Nurilla Avazov and Matthias Pätzold
Faculty of Engineering and Science, University of Agder,
P.O. Box 509, NO-4898 Grimstad, Norway
E-mails: {nurilla.k.avazov, matthias.paetzold}@uia.no

Abstract — **This paper presents a geometric street scattering channel model for car-to-car (C2C) communication systems under line-of-sight (LOS) and non-LOS (NLOS) propagation conditions. Starting from the geometric model, we develop a stochastic reference channel model, where the scatterers are uniformly distributed in rectangles in the form of stripes parallel to both sides of the street. We derive analytical expressions for the probability density functions (PDFs) of the angle-of-departure (AOD) and the angle-of-arrival (AOA). We also investigate the Doppler power spectral density (PSD) and the autocorrelation function (ACF) of the proposed model, assuming that the mobile transmitter (MT) and the mobile receiver (MR) are moving, while the surrounding scatterers are fixed. To validate the reference channel model, its Doppler parameters are compared to those of a real-world measured channel for urban and rural areas. The numerical results show a good fitting of the theoretical results to the computer simulations. The proposed geometry-based channel model allows to study the effects of the street scatterers on the performance of C2C communication systems.**

I. INTRODUCTION

C2C communications have recently received great attention due to some traffic telematic applications that make transportation safer, more efficient, and more environmentally friendly [1]. Robust and reliable traffic telematic applications and services require C2C wireless communication systems that can provide robust connectivity. To develop such wireless communication systems and standards, accurate channel models for the C2C communication systems are required. In this context, several mobile-to-mobile (M2M) fading channels have been proposed, for example, one-ring [2], two-ring [3], and elliptical [4] channel models. A two-dimensional (2D) reference model for a single-input single-output (SISO) M2M Rayleigh fading channel has been proposed by Akki and Haber in [5]. In [6], a three-dimensional (3D) model for wideband multiple-input multiple-output (MIMO) M2M channel is studied. Its corresponding first- and second-order channel statistics have been investigated and validated by using an experimental MIMO M2M channel sounding campaign.

In C2C communication systems, the transmitter and the receiver are in motion, in this respect the underlying radio channel model differs from the traditional cellular channels. Consequently, new channel models are required for C2C communication systems. For instance, several geometry-based street models have been studied and analyzed in [7–10]. Especially, the T-junction model has widely been investigated by assuming different scattering scenarios. In [7], a geometry-based channel model has been proposed, where scatterers are located in one line. A non-stationary MIMO vehicular-to-vehicular (V2V) channel model based on the T-junction model has been derived in [8]. The proposed channel model takes into account double-bounced scattering from fixed scatterers. To study the statistical properties of the proposed channel model, the Choi-Williams distribution has been used. In [11], a GPS-enabled channel sounding platform for measuring V2V wireless channels under LOS and NLOS propagation conditions has been presented.

In the literature, a number of fundamental channel models with different scatterer distributions, e.g., uniform, Gaussian, Laplacian, and von Mises, have been used to characterize the AOD and AOA. For example, in [12] the author discusses a Gaussian scatterer distribution model by assuming a circular scattering region around a mobile station. It has also been analyzed the spatial and temporal properties of the first arrival path in multipath environments. The authors of [13] and [14] focused on the modeling of narrowband and wideband SISO mobile fading channels for indoor radio propagation environments, respectively. It has been assumed that scatterers are uniformly distributed in the 2D horizontal plane of a room. The

base station is considered as the transmitter while the mobile station is the receiver.

In contrast to [13], in this paper, we propose a new geometric street scattering channel model for outdoor propagation environments, while both the MT and the MR are in motion. The main contribution of this paper is that it presents a geometric street model with an infinite number of scatterers, which are uniformly distributed in rectangles in the form of stripes parallel to both sides of the street. A typical propagation scenario for the proposed model is shown in Fig. A.1, where the buildings and the trees can be considered as scatterers. The analytical expressions for the PDFs of the AOD and the AOA, as well as the transmitter and the receiver Doppler frequencies have been derived. We have also investigated the Doppler PSD and the ACF of the proposed model. To confirm the correctness of the proposed model, the Doppler parameters of the reference model have been compared to those of the measured channel in [11]. The numerical results show that the statistics of the proposed model fit very well to those of the computer simulations.

The rest of this paper is organized as follows. Section II describes the geometric street scattering model. In Section III, the reference channel model is reviewed. We also study the statistical properties of the proposed geometry-based street scattering model, such as the PDFs of the AOD and the AOA. In Section IV, the parameters of a measurement-based model have been computed. The evaluation of the main statistical properties of the proposed model is the topic of Section V. Finally, Section VI provides the conclusion of the paper.

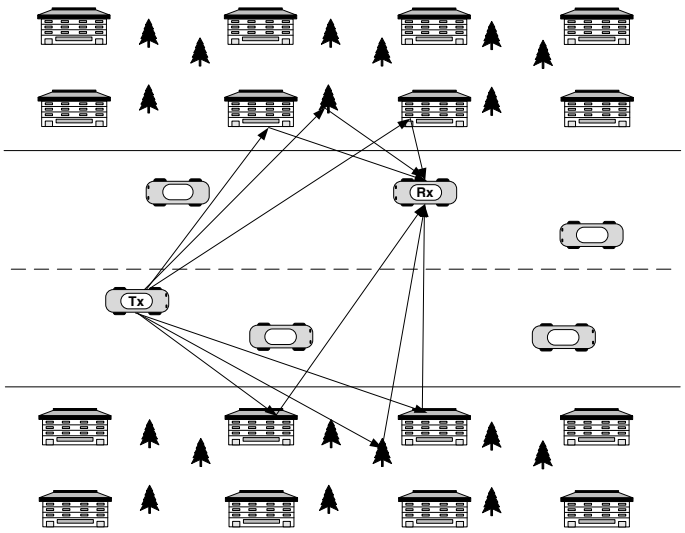

Figure A.1: A typical propagation scenario at a straight street.

II. The Geometric Street Scattering Model

We consider the geometric street scattering model as depicted in Fig. A.2. In our model, the geometric street scattering model describes the scattering environment for an M2M channel, which constitutes the starting point for the derivation of the reference model. We consider rectangle areas at both sides of the street with length A_i $(i = 1,2)$ and width B_i $(i = 1,2)$. The MT and the MR are placed in the street with distance D, denoted by $D = x_R + x_T$. We assume that the MT with coordinates (x_T, y_T), moving with speed v_T in the direction of the x-axis, is communicating with the MR with coordinates (x_R, y_R), moving with speed v_R in the opposite direction of the x-axis. The transmitter (receiver) is located at a distance y_{T_1} (y_{R_1}) from the left-hand side of the street and at a distance y_{T_2} (y_{R_2}) from the right-hand side of the street. The symbols α and β stand for the AOD and the AOA, respectively.

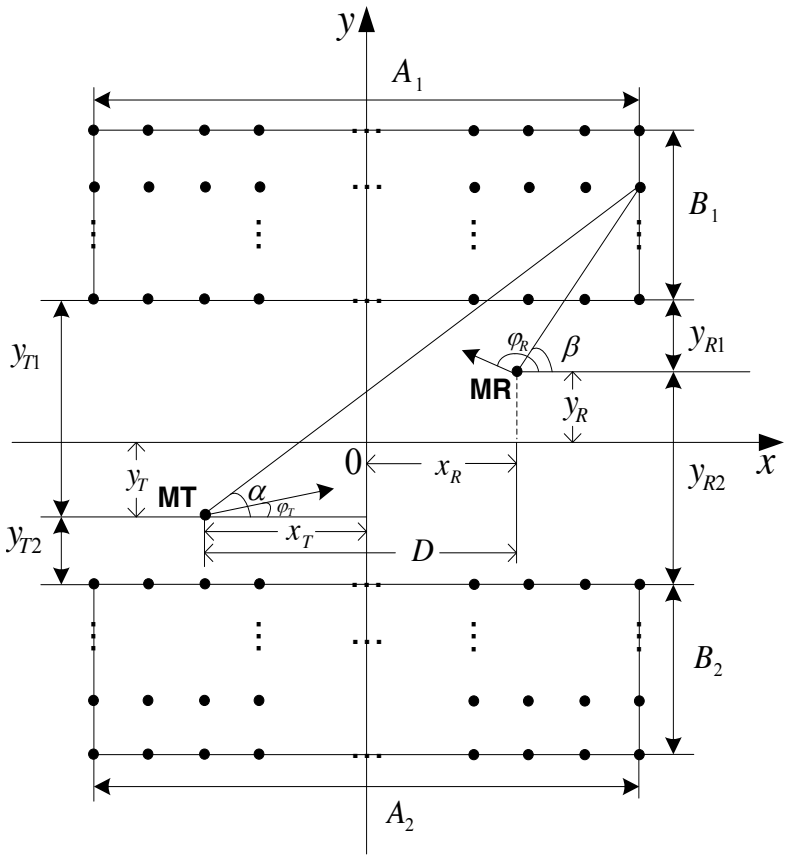

Figure A.2: Geometric street scattering model with local scatterers uniformly distributed in the rectangles at both sides of the street.

III. The Geometric Street Scattering Channel Model and Its Statistical Properties

In this section, we first review the reference channel model of M2M communication systems under LOS and NLOS propagation conditions. Then, we derive the PDFs of the AOD and the AOA. Thereafter, by using the PDFs of the AOD and the AOA, we obtain the PDFs of the transmitter and the receiver Doppler frequencies, as well as the total Doppler frequency, which enables us to analyze the Doppler PSD of the proposed geometric street scattering channel model.

A. Review of the Reference Channel Model

The reference channel model can be modeled by a complex process

$$\mu_\rho(t) = \mu(t) + m(t) \tag{A.1}$$

where $\mu(t)$ denotes the sum of the scattered components and $m(t)$ represents the LOS part. The LOS part of the received signal can generally be described by a complex sinusoid (cisoid) of the form [14]

$$m(t) = \rho e^{j(2\pi f_\rho t + \theta_\rho)}, \tag{A.2}$$

where ρ, f_ρ, and θ_ρ denote the amplitude, the Doppler frequency, and the phase of the LOS part, respectively. If not otherwise stated, then it is supposed that the parameters ρ, f_ρ, and θ_ρ are constant; meaning that the LOS part $m(t)$ is a time-variant deterministic process.

Usually, it is assumed that the real and imaginary part of the scattered component $\mu(t)$ are zero-mean Gaussian processes, each having the variance $\sigma_\mu^2/2$. The absolute value of $\mu_\rho(t)$ in (A.1) leads to the Rice process, i.e., $\xi(t) = |\mu_\rho(t)|$. Under NLOS conditions the Rice process $\xi(t)$ reduces to the Rayleigh process, i.e., $\zeta(t) = |\mu(t)|$ [15].

B. Derivation of the PDFs of the AOD and the AOA

We use boldface letters to denote random variables and normal letters for the values that the corresponding random variable can take. Let us assume that in Fig. A.2 the position of all scatterers in the rectangle is presented by (x,y). The positions of the MT and the MR are denoted by (x_T, y_T) and (x_R, y_R), respectively, each having non-zero positive value. Accordingly, the AOD $\boldsymbol{\alpha}$ and the AOA $\boldsymbol{\beta}$ can be expressed

as

$$\boldsymbol{\alpha} = \begin{cases} \arctan\frac{\boldsymbol{y}+y_T}{\boldsymbol{x}+x_T}, & \text{if } \boldsymbol{x} \geq -x_T, \\ \pi + \arctan\frac{\boldsymbol{y}+y_T}{\boldsymbol{x}+x_T}, & \text{if } \boldsymbol{x} < -x_T \text{ and } \boldsymbol{y} \geq -y_T, \\ -\pi + \arctan\frac{\boldsymbol{y}+y_T}{\boldsymbol{x}+x_T}, & \text{if } \boldsymbol{x} > -x_T \text{ and } \boldsymbol{y} < -y_T, \end{cases} \tag{A.3}$$

$$\boldsymbol{\beta} = \begin{cases} \arctan\frac{\boldsymbol{y}-y_R}{\boldsymbol{x}-x_R}, & \text{if } \boldsymbol{x} \geq x_R \\ \pi + \arctan\frac{\boldsymbol{y}-y_R}{\boldsymbol{x}-x_R}, & \text{if } \boldsymbol{x} < x_R \text{ and } \boldsymbol{y} \geq y_R, \\ -\pi + \arctan\frac{\boldsymbol{y}-y_R}{\boldsymbol{x}-x_R}, & \text{if } \boldsymbol{x} > x_R \text{ and } \boldsymbol{y} < y_R\,. \end{cases} \tag{A.4}$$

For ease of analysis of the AOD and the AOA, we shift the origin of the coordinate system to the positions where the MT and the MR are located in Figs. (A.3a) and in (A.3b), respectively. We introduce new coordinate systems for the MT and the MR, where we have $\boldsymbol{x}' = \boldsymbol{x} + x_T$, $\boldsymbol{y}' = \boldsymbol{y} + y_T$ and $\boldsymbol{x}'' = \boldsymbol{x} - x_R$, $\boldsymbol{y}'' = \boldsymbol{y} - y_R$, respectively.

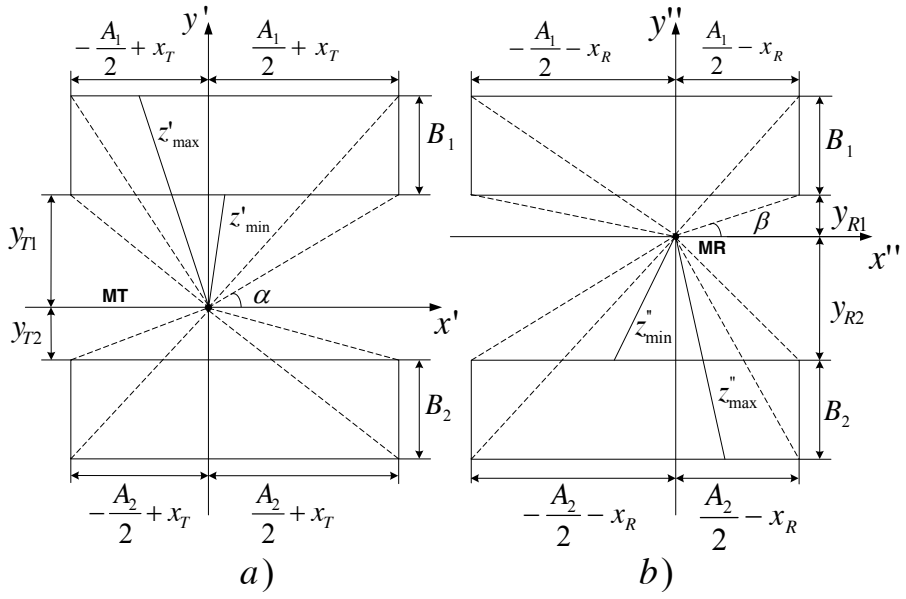

Figure A.3: Geometric street scattering model: Illustrating a) the AOD α and b) the AOA β.

It is mentioned in Section II that all scatterers are uniformly distributed in the rectangle areas at both sides of the street. Hence, the random variables $\boldsymbol{x}'$ and $\boldsymbol{x}''$ are also uniformly distributed over the ranges $[-A_i/2+x_T, A_i/2+x_T]$, $(i=1,2)$ and $[-A_i/2-x_R, A_i/2-x_R]$, $(i=1,2)$, respectively; while $\boldsymbol{y}'$ and $\boldsymbol{y}''$ follow the uniform distribution in the intervals $[y_{T_1}, B_1+y_{T_1}] \cup [-B_2-y_{T_2}, -y_{T_2}]$ and $[y_{R_1}, B_1+y_{R_1}] \cup [-B_2-y_{R_2}, -y_{R_2}]$, respectively. Thus, the densities $p_{\boldsymbol{x}'}(x')$, $p_{\boldsymbol{x}''}(x'')$, $p_{\boldsymbol{y}'}(y')$, and

$p_{\boldsymbol{y}''}(y'')$ of $\boldsymbol{x}'$, $\boldsymbol{x}''$, $\boldsymbol{y}'$, and $\boldsymbol{y}''$, respectively, are given by

$$p_{\boldsymbol{x}'}(x') = \frac{1}{A_i}, \quad \text{if} \quad \boldsymbol{y}' \in I_i,\ i = 1,2, \tag{A.5}$$

$$p_{\boldsymbol{x}''}(x'') = \frac{1}{A_i}, \quad \text{if} \quad \boldsymbol{y}'' \in J_i,\ i = 1,2, \tag{A.6}$$

$$p_{\boldsymbol{y}'}(y') = p_{\boldsymbol{y}''}(y'') = \frac{1}{B_1 + B_2}, \tag{A.7}$$

where $I_1 = [y_{T_1}, B_1 + y_{T_1}]$, $I_2 = [-B_2 - y_{T_2}, -y_{T_2}]$, $J_1 = [y_{R_1},\ B_1 + y_{R_1}]$, and $J_2 = [-B_2 - y_{R_2}, -y_{R_2}]$. Assuming that the random variables $\boldsymbol{x}'$, $\boldsymbol{x}''$, $\boldsymbol{y}'$, and $\boldsymbol{y}''$ are independent, the joint PDFs $p_{\boldsymbol{x}'\boldsymbol{y}'}(x', y') = p_{\boldsymbol{x}'}(x') \cdot p_{\boldsymbol{y}'}(y')$ and $p_{\boldsymbol{x}''\boldsymbol{y}''}(x'', y'') = p_{\boldsymbol{x}''}(x'') \cdot p_{\boldsymbol{y}''}(y'')$ of the random variables $\boldsymbol{x}'$, $\boldsymbol{y}'$ and $\boldsymbol{x}''$, $\boldsymbol{y}''$, respectively, can be expressed as

$$p_{\boldsymbol{x}'\boldsymbol{y}'}(x', y') = \frac{1}{A_i(B_1 + B_2)}, \quad \text{if} \quad \boldsymbol{y}' \in I_i,\ i = 1,2, \tag{A.8}$$

$$p_{\boldsymbol{x}''\boldsymbol{y}''}(x'', y'') = \frac{1}{A_i(B_1 + B_2)}, \quad \text{if} \quad \boldsymbol{y}'' \in J_i,\ i = 1,2. \tag{A.9}$$

The transformation of the Cartesian coordinates (x', y') and (x'', y'') into polar coordinates (z', α) and (z'', β) gives the joint PDFs $p_{\boldsymbol{z}'\boldsymbol{\alpha}}(z', \alpha)$ and $p_{\boldsymbol{z}''\boldsymbol{\beta}}(z'', \beta)$ of $\boldsymbol{z}' = \sqrt{(\boldsymbol{x}'^2 + \boldsymbol{y}'^2)}$ and $\boldsymbol{z}'' = \sqrt{(\boldsymbol{x}''^2 + \boldsymbol{y}''^2)}$ with the corresponding AOD $\boldsymbol{\alpha} = \arctan(\boldsymbol{y}'/\boldsymbol{x}')$ and AOA $\boldsymbol{\beta} = \arctan(\boldsymbol{y}''/\boldsymbol{x}'')$, respectively. Hence, the joint PDFs $p_{\boldsymbol{z}'\boldsymbol{\alpha}}(z', \alpha)$ and $p_{\boldsymbol{z}''\boldsymbol{\beta}}(z'', \beta)$ can be expressed as

$$p_{\boldsymbol{z}'\boldsymbol{\alpha}}(z', \alpha) = \frac{z'}{A_i(B_1 + B_2)}, \quad \text{if} \quad \boldsymbol{y}' \in I_i,\ i = 1,2, \tag{A.10}$$

$$p_{\boldsymbol{z}''\boldsymbol{\beta}}(z'', \beta) = \frac{z''}{A_i(B_1 + B_2)}, \quad \text{if} \quad \boldsymbol{y}'' \in J_i,\ i = 1,2. \tag{A.11}$$

By integrating the joint PDFs $p_{\boldsymbol{z}'\boldsymbol{\alpha}}(z', \alpha)$ and $p_{\boldsymbol{z}''\boldsymbol{\alpha}}(z'', \alpha)$ over z' and z'', respectively, we obtain the PDFs of the AOD $\boldsymbol{\alpha}$ and AOA $\boldsymbol{\beta}$, respectively, as

$$p_{\boldsymbol{\alpha}}(\alpha) = \frac{{z'_{\max}}^2}{2A_i(B_1 + B_2)} - \frac{{z'_{\min}}^2}{2A_i(B_1 + B_2)}, \tag{A.12}$$

$$p_{\boldsymbol{\beta}}(\beta) = \frac{{z''_{\max}}^2}{2A_i(B_1 + B_2)} - \frac{{z''_{\min}}^2}{2A_i(B_1 + B_2)}, \tag{A.13}$$

where $z'_{\max}$, $z'_{\min}$ (see Fig. (A.3a)), $z''_{\max}$, and $z''_{\min}$ (see Fig. (A.3b)) stand for the distance from the origin to the boundaries of the rectangle area.

Using the geometrical relationships, we derive an expression for $z'_{\max}$, $z'_{\min}$, $z''_{\max}$, and $z''_{\min}$ in form of a piecewise function depending on the AOD α and the AOA β,

respectively, and A_i, B_i. The AOD and AOA ranges are separated by dash lines in Figs. (A.3a) and (A.3b), respectively. For brevity, we only present here the final expressions for the PDFs of the AOD $\boldsymbol{\alpha}$ in (A.31) and the AOA $\boldsymbol{\beta}$ in (A.32), which can be found in Appendix A.A.

C. Derivation of the PDFs of the Transmitter and the Receiver Doppler Frequencies

Due to the assumption that the AOD $\boldsymbol{\alpha}$ and the AOA $\boldsymbol{\beta}$ are random variables, it follows that the corresponding transmitter and receiver Doppler frequencies defined by

$$\boldsymbol{f}_T = f_T(\boldsymbol{\alpha}) = f_{T_{\max}} \cos(\boldsymbol{\alpha} - \varphi_T), \tag{A.14}$$

$$\boldsymbol{f}_R = f_R(\boldsymbol{\beta}) = f_{R_{\max}} \cos(\boldsymbol{\beta} - \varphi_R), \tag{A.15}$$

are also random variables. The quantities $f_{T_{\max}}$ and $f_{R_{\max}}$ stand for the maximum Doppler frequencies of the transmitter and receiver, respectively, while φ_T, and φ_R denote the angles between the direction of the transmitter and receiver w.r.t the x-axis, respectively.

The PDFs of the Doppler frequencies $\boldsymbol{f}_T$ and $\boldsymbol{f}_R$, denoted by $p_{\boldsymbol{f}_T}(f_T)$ and $p_{\boldsymbol{f}_R}(f_R)$, respectively, can easily be computed by using the fundamental theorem of transformation of random variables [16]. Consequently, the PDFs $p_{\boldsymbol{f}_T}(f_T)$ and $p_{\boldsymbol{f}_R}(f_R)$ can be defined as

$$p_{\boldsymbol{f}_T}(f_T) = \sum_{l=1}^{m} \frac{p_{\boldsymbol{\alpha}}(\alpha)}{|\frac{\partial}{\partial \alpha}|_{\alpha=\alpha_l}} \tag{A.16}$$

$$p_{\boldsymbol{f}_R}(f_R) = \sum_{u=1}^{v} \frac{p_{\boldsymbol{\beta}}(\beta)}{|\frac{\partial}{\partial \beta}|_{\beta=\beta_u}}, \tag{A.17}$$

where m and v are the number of the solutions of the equations in (A.16) and (A.17), respectively, within the interval $[-\pi, \pi)$. If $f_T \leq |f_{T_{\max}}|$ and $f_R \leq |f_{R_{\max}}|$, we find two real-valued solutions within the interval, which are known as

$$\alpha_1 = -\alpha_2 = \arccos(\frac{f_T}{f_{T_{\max}}}) + \varphi_T, \tag{A.18}$$

$$\beta_1 = -\beta_2 = \arccos(\frac{f_R}{f_{R_{\max}}}) + \varphi_R, \tag{A.19}$$

so that $m = 2$ and $v = 2$. After some mathematical computations and by using (A.14)-(A.19), we find the following results for the PDFs $p_{\boldsymbol{f}_T}(f_T)$ and $p_{\boldsymbol{f}_R}(f_R)$

$$p_{\boldsymbol{f}_T}(f_T) = \frac{p_{\boldsymbol{\alpha}}(\alpha_1) + p_{\boldsymbol{\alpha}}(\alpha_2)}{\sqrt{f_{T_{\max}}^2 - f_T^2}} \, |_{\alpha_1=-\alpha_2}, \tag{A.20}$$

$$p_{\boldsymbol{f}_R}(f_R) = \frac{p_{\boldsymbol{\beta}}(\beta_1)+p_{\boldsymbol{\beta}}(\beta_2)}{\sqrt{f_{R_{\max}}^2 - f_R^2}} \,|_{\beta_1=-\beta_2}\,. \tag{A.21}$$

The final expressions for the densities $p_{\boldsymbol{f}_T}(f_T)$ [see (A.33)] and $p_{\boldsymbol{f}_R}(f_R)$ [see (A.34)] are given in Appendix A.A.

Now, we introduce the total Doppler frequency, defined by $\boldsymbol{f} = \boldsymbol{f}_T + \boldsymbol{f}_R$, of the geometric street scattering model. Consequently, the PDF $p_{\boldsymbol{f}}(f)$ of the sum $\boldsymbol{f} = \boldsymbol{f}_T + \boldsymbol{f}_R$ of two independent random variables, $\boldsymbol{f}_T$ and $\boldsymbol{f}_R$ is equal to the convolution of their densities. To obtain the PDF $p_{\boldsymbol{f}}(f)$ of $\boldsymbol{f}$ we use the characteristic functions $\Phi_{\boldsymbol{f}_T}(\omega)$ and $\Phi_{\boldsymbol{f}_R}(\omega)$ of $\boldsymbol{f}_T$ and $\boldsymbol{f}_R$, respectively, which are defined as

$$\Phi_{\boldsymbol{f}_T}(\omega) = E\left\{e^{j\omega \boldsymbol{f}_T}\right\} = \int_{-\infty}^{\infty} p_{\boldsymbol{f}_T}(f_T) e^{j\omega f_T} df_T\,, \tag{A.22}$$

$$\Phi_{\boldsymbol{f}_R}(\omega) = E\left\{e^{j\omega \boldsymbol{f}_R}\right\} = \int_{-\infty}^{\infty} p_{\boldsymbol{f}_R}(f_R) e^{j\omega f_R} df_R\,. \tag{A.23}$$

By using (A.22) and (A.23), we can find the characteristic function $\Phi_{\boldsymbol{f}}(\omega)$ of the total Doppler frequency $\boldsymbol{f}$ by the product of two characteristic functions as

$$\Phi_{\boldsymbol{f}}(\omega) = \Phi_{\boldsymbol{f}_T}(\omega) \cdot \Phi_{\boldsymbol{f}_R}(\omega)\,. \tag{A.24}$$

Consequently, by using the Fourier transform inversion formula for (A.24), we can derive the PDF $p_{\boldsymbol{f}}(f)$ of $\boldsymbol{f}$ as

$$p_{\boldsymbol{f}}(f) = \frac{1}{2\pi} \int_{-\infty}^{\infty} \Phi_{\boldsymbol{f}}(\omega) e^{-j\omega f} d\omega\,. \tag{A.25}$$

Since no closed-form solution exists for the PDF $p_{\boldsymbol{f}}(f)$ in (A.25), this integral has to be solved numerically.

D. Derivation of the Doppler PSD and the ACF

The Doppler PSD $S_{\mu_\rho\mu_\rho}(f)$ of the process $\mu_\rho(t)$ in (A.1) can be presented as,

$$S_{\mu_\rho\mu_\rho}(f) = S_{\mu\mu}(f) + \rho^2 \delta(f - f_\rho) \tag{A.26}$$

which is the sum of the Doppler PSD $S_{\mu\mu}(f)$ of $\mu(t)$ and a weighted delta function at $f = f_\rho$. In our model, we consider that the number of scatterers is infinite; therefore, the Doppler PSD $S_{\mu\mu}(f)$ of the scattered component $\mu(t)$ is continuous. According to [15], the mean power within an infinitesimal frequency interval

df can be represented by $S_{\mu\mu}(f)df$. Therefore, due to $\int_{-\infty}^{\infty} S_{\mu\mu}(f)df = \sigma_\mu^2$ and $\int_{-\infty}^{\infty} p_{\boldsymbol{f}}(f)df = 1$, it follows the relation

$$S_{\mu\mu}(f) = \sigma_\mu^2 p_{\boldsymbol{f}}(f). \tag{A.27}$$

By taking (A.27) into account and using (A.31), (A.32), (A.33), (A.34), and (A.25) we compute the Doppler PSD $S_{\mu\mu}(f)$ of $\mu(t)$. Thus, the Doppler PSD $S_{\mu_\rho\mu_\rho}(f)$ of $\mu_\rho(t)$ can easily be derived by substituting (A.27) into (A.26).

From the $S_{\mu\mu}(f)$, we can directly compute the ACF of the scattered components $\mu(t)$ by taking the inverse Fourier transform of the Doppler PSD $S_{\mu\mu}(f)$, i.e., $r_{\mu\mu}(\tau) = \int_{-\infty}^{\infty} S_{\mu\mu}(f)e^{j2\pi f\tau}df$. Consequently, we can express the ACF $r_{\mu_\rho\mu_\rho}(\tau)$ in terms of the ACF $r_{\mu\mu}(\tau)$ of $\mu(t)$ as follows

$$r_{\mu_\rho\mu_\rho}(\tau) = r_{\mu\mu}(\tau) + \rho^2 e^{j2\pi f_\rho \tau}. \tag{A.28}$$

IV. Measurement-Based Model Parameters

The objective of this section is to compute the model parameters A_i, B_i, y_{Ti}, y_{Ri}, $(i = 1,2)$, x_R, x_T, $f_{T_{\max}}$, and $f_{R_{\max}}$ such that the average Doppler shift $B^{(1)}_{\mu_\rho\mu_\rho}$ and the Doppler spread $B^{(2)}_{\mu_\rho\mu_\rho}$ of the reference model are close to those $\left(B^{\star(1)}_{\mu_\rho\mu_\rho}\right.$ and $\left.B^{\star(2)}_{\mu_\rho\mu_\rho}\right)$ of the measured channel reported in [11]. To solve this parameter computation problem, we compute the model parameters such that the following errors

$$E_{B^{(1)}_{\mu_\rho\mu_\rho}} = \left|B^{\star(1)}_{\mu_\rho\mu_\rho} - B^{(1)}_{\mu_\rho\mu_\rho}\right| \tag{A.29}$$

$$E_{B^{(2)}_{\mu_\rho\mu_\rho}} = \left|B^{\star(2)}_{\mu_\rho\mu_\rho} - B^{(2)}_{\mu_\rho\mu_\rho}\right| \tag{A.30}$$

become a minimum. Finally, measurement-based model parameters and the corresponding Doppler parameters are listed in Table A.1.

V. Numerical Results

In this section, we will discuss the main theoretical results by evaluating the Doppler PSD and the ACF of the proposed model. We consider a rectangle area at both sides of the street with length $A_1 = A_2 = 200$ m and width $B_1 = B_2 = 40$ m as our outdoor street model. All theoretical results have been obtained by choosing $\sigma^2_{\mu_\rho} = \sigma^2_\mu + \rho^2 = 1$, $f_\rho = 65$ Hz, $\theta_\rho = 0^\circ$, $\varphi_T = 0^\circ$, $\varphi_R = 180^\circ$, and $f_{\max} = 182$ Hz. The Rice factor $c_R = \rho^2/\sigma^2_\mu$ was chosen from the set $\{0,2,4\}$.

The theoretical results for the Doppler PSD $S_{\mu\mu}(f)$ in (A.27) of the channel's scattered component $\mu(t)$ are presented in Figs. A.4 and A.5 for the different length

Table A.1: Measurement-based parameters of the geometrical street scattering channel model and its Doppler statistics.

Model parameters	**Propagation Environment**		
	Urban LOS	**Urban NLOS**	**Rural LOS**
A_1 (A_2) (m)	993 (992)	1027 (1007)	1014 (957)
B_1 (B_2) (m)	50 (50)	51 (50)	5 (5)
$f_{T_{\max}}$ $(f_{R_{\max}})$ (Hz)	165 (165)	144 (164)	523 (574)
x_T (x_R) (m)	101 (103)	109 (169)	51 (51)
y_{T1} (y_{T2}) (m)	12 (8)	13 (8)	12 (8)
y_{R1} (y_{R2}) (m)	8 (12)	8 (12)	8 (12)
ρ^2	0.8	-	0.8
f_ρ (Hz)	65	-	66
σ_μ^2	0.2	-	0.2
Measured average Doppler shift $B^{\star(1)}_{\mu_\rho\mu_\rho}$ (Hz)	-20 [11]	103 [11]	201 [11]
Theoretical average Doppler shift $B^{(1)}_{\mu_\rho\mu_\rho}$ (Hz)	-20	103	201

Model parameters	**Propagation Environment**		
	Urban LOS	**Urban NLOS**	**Rural LOS**
A_1 (A_2) (m)	3814 (3446)	418 (421)	1206 (1399)
B_1 (B_2) (m)	46 (43)	51 (47)	5 (5)
$f_{T_{\max}}$ $(f_{R_{\max}})$ (Hz)	164 (153)	152 (162)	482 (581)
x_T (x_R) (m)	105 (93)	209 (386)	51 (52)
y_{T1} (y_{T2}) (m)	12 (8)	3 (12)	12 (8)
y_{R1} (y_{R2}) (m)	7 (12)	7 (8)	8 (12)
ρ^2	0.9	-	0.8
f_ρ (Hz)	59	-	67
σ_μ^2	0.2	-	0.2
Measured Doppler spread $B^{\star(2)}_{\mu_\rho\mu_\rho}$ (Hz)	341 [11]	298 [11]	782 [11]
Theoretical Doppler spread $B^{(2)}_{\mu_\rho\mu_\rho}$ (Hz)	340.9	298	780

and width of the rectangles at both sides of the street. Figure A.4 illustrates that by increasing the length $A_i,\ (i=1,2)$, the shape of the Doppler PSD at $f>0$ becomes a U shape. The Doppler PSD $S_{\mu\mu}$ for different values of the area width $B_i,\ (i=1,2)$

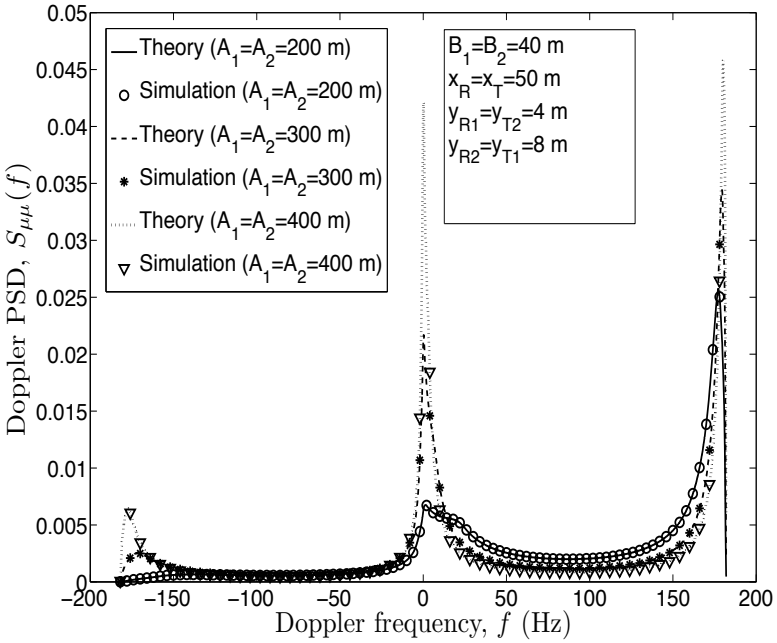

Figure A.4: Doppler PSD $S_{\mu\mu}(f)$ of $\mu(t)$ for different values of the area length $A_1=A_2$ ($B_1=B_2=40$ m, $x_R=x_T=50$ m, $y_{R1}=y_{T2}=4$ m, and $y_{R2}=y_{T1}=8$ m).

are demonstrated in Fig. A.5. It shows that for different B_i values, the Doppler PSD gets its maximum peaks at $f = f_{\max}$. The shape of the Doppler PSD resembles a Gaussian shape when the length of B_i is very large.

The theoretical results demonstrated in Figs. A.4 and A.5 are also confirmed by simulations. In the simulation, we generate the scatterers, which are uniformly randomly distributed in the rectangles. The locations of the scatterers have been determined by outcomes of a random generator with uniform distribution in the intervals $[-A_i/2+x_T, A_i/2+x_T]$, $(i=1,2)$ ($[-A_i/2-x_R, A_i/2-x_R]$, $(i=1,2)$) and $[y_{T_1}, B_1+y_{T_1}]\cup[-B_2-y_{T_2}, -y_{T_2}]$ ($[y_{R_1}, B_1+y_{R_1}]\cup[-B_2-y_{R_2}, -y_{R_2}]$). By using (A.3), (A.4), (A.14), and (A.15), we can obtained the densities of the transmitter (receiver) Doppler frequencies. Thereafter, we can find the total Doppler frequencies, i.e., $f=f_T+f_R$. Finally, we can numerically compute the Doppler PSD by means of (A.27).

Figure A.6 shows the absolute value of the ACF $r_{\mu_\rho\mu_\rho}(\tau)$ of the process $\mu_\rho(t)$ by considering different values for the Rice factor c_R. As shown in Fig. A.6, under NLOS condition ($c_R=0$) the curve of the ACF fluctuates with less peaks by gradually decreasing while the time lag increases. The obtained theoretical results in Fig.

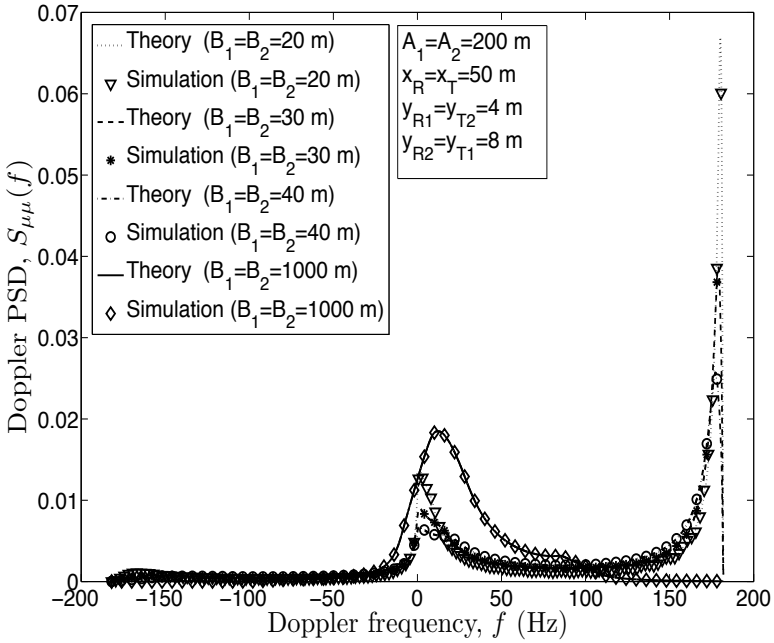

Figure A.5: Doppler PSD $S_{\mu\mu}(f)$ of $\mu(t)$ for different values of the area width $B_1 = B_2$ ($A_1 = A_2 = 200$ m, $x_R = x_T = 50$ m, $y_{R1} = y_{T2} = 4$ m, and $y_{R2} = y_{T1} = 8$ m).

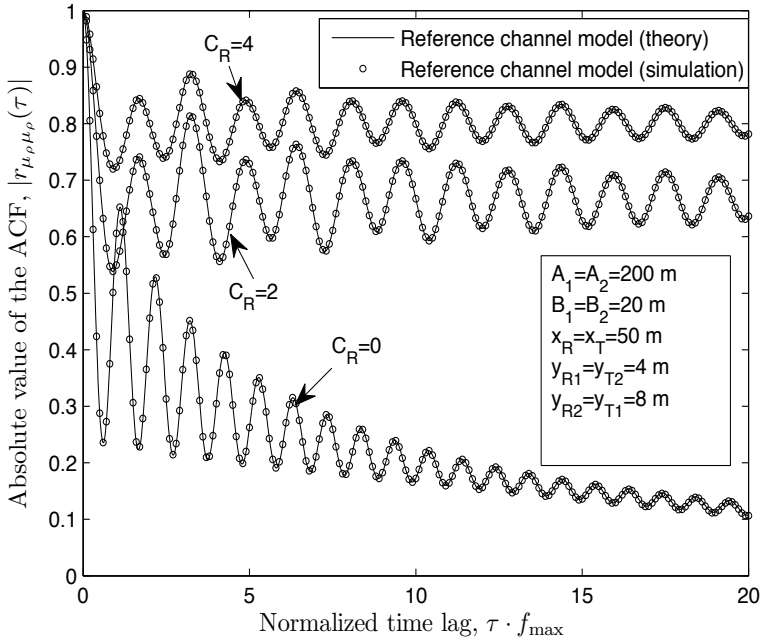

Figure A.6: The absolute value of the ACF $r_{\mu_\rho\mu_\rho}(\tau)$ of the reference channel model ($A_1 = A_2 = 200$ m, $B_1 = B_2 = 20$ m, $x_R = x_T = 50$ m, $y_{R1} = y_{T2} = 4$ m, and $y_{R2} = y_{T1} = 8$ m).

A.6 have also been confirmed by computer simulations.

VI. Conclusion

We designed the geometric street scattering channel model with local scatterers, which are uniformly distributed in the rectangles in the form of stripes parallel to both sides of the street. We have derived analytical expressions for the PDFs of the AOD (AOA) and the transmitter (receiver) Doppler frequencies. By obtaining the PDF of the total Doppler frequency, we have numerically computed the Doppler PSD and the ACF of the proposed geometric street scattering model. For the different size of scattering ranges we have studied the Doppler PSD of the proposed model. We have also validated our model by fitting the Doppler parameters of the reference model to those of the measured one. Numerical results show that the theoretical results of the proposed model fit very well to the computer simulations. To design an efficient C2C channel model, the properties of the wireless multipath environments are of great importance. Therefore, the distribution behavior of the scatterers and scattering regions play a key role in the design of future C2C communication systems.

APPENDIX A.A

In this appendix, we provide the final results for the PDFs of the AOD $\boldsymbol{\alpha}$ and the AOA $\boldsymbol{\beta}$, as well as the transmitter and the receiver Doppler frequencies $\boldsymbol{f}_T$ and $\boldsymbol{f}_R$, respectively.

THE FINAL EXPRESSIONS FOR THE PDFS OF THE AOD $\boldsymbol{\alpha}$ AND THE AOA $\boldsymbol{\beta}$

$$p_{\boldsymbol{\alpha}}(\alpha)=\begin{cases}\frac{(A_1+2x_T)^2}{4A_1g_1(\alpha)}-\frac{y_{T1}^2}{A_1g_2(\alpha)}, & \text{if } \arctan\frac{2y_{T1}}{A_1+2x_T}<\alpha\leq\arctan\frac{2B_1+2y_{T1}}{A_1+2x_T}\\ \frac{(B_1+y_{T1})^2}{A_1g_2(\alpha)}-\frac{y_{T1}^2}{A_1g_2(\alpha)}, & \text{if } \arctan\frac{2B_1+2y_{T1}}{A_1+2x_T}<\alpha\leq\pi-\arctan\frac{2B_1+2y_{T1}}{A_1-2x_T}\\ \frac{(A_1-2x_T)^2}{4A_1g_1(\alpha)}-\frac{y_{T1}^2}{A_1g_2(\alpha)}, & \text{if } \pi-\arctan\frac{2B_1+2y_{T1}}{A_1-2x_T}<\alpha\leq\pi-\arctan\frac{2y_{T1}}{A_1-2x_T}\\ \frac{(A_2-2x_T)^2}{4A_2g_1(\alpha)}-\frac{y_{T2}^2}{A_2g_2(\alpha)}, & \text{if } -\pi+\arctan\frac{2y_{T2}}{A_2-2x_T}<\alpha\leq-\pi+\arctan\frac{2B_2+2y_{T2}}{A_2-2x_T}\\ \frac{(B_2+y_{T2})^2}{A_2g_2(\alpha)}-\frac{y_{T2}^2}{A_2g_2(\alpha)}, & \text{if } -\pi+\arctan\frac{B_2+2y_{T2}}{A_2-2x_T}<\alpha\leq-\arctan\frac{2B_2+2y_{T2}}{A_2+2x_T}\\ \frac{(A_2+2x_T)^2}{4A_2g_1(\alpha)}-\frac{y_{T2}^2}{A_2g_2(\alpha)}, & \text{if } -\arctan\frac{2B_2+2y_{T2}}{A_2+2x_T}<\alpha\leq-\arctan\frac{2y_{T2}}{A_2+2x_T}\end{cases} \tag{A.31}$$

where $g_1(\alpha)=2(B_1+B_2)\cos^2(\alpha)$ and $g_2(\alpha)=2(B_1+B_2)\sin^2(\alpha)$.

$$p_{\boldsymbol{\beta}}(\beta)=\begin{cases}\frac{(A_1-2x_R)^2}{4A_1g_1(\beta)}-\frac{y_{R1}^2}{A_1g_2(\beta)}, & \text{if } \arctan\frac{2y_{R1}}{A_1-2x_R}<\beta\leq\arctan\frac{2B_1+2y_{R1}}{A_1-2x_R}\\ \frac{(B_1+y_{R1})^2}{A_1g_2(\beta)}-\frac{y_{R1}^2}{A_1g_2(\beta)}, & \text{if } \arctan\frac{2B_1+2y_{R1}}{A_1-2x_R}<\beta\leq\pi-\arctan\frac{2B_1+2y_{R1}}{A_1+2x_R}\\ \frac{(A_1+2x_R)^2}{4A_1g_1(\beta)}-\frac{y_{R1}^2}{A_1g_2(\beta)}, & \text{if } \pi-\arctan\frac{2B_1+2y_{R1}}{A_1+2x_R}<\beta\leq\pi-\arctan\frac{2y_{R1}}{A_1+2x_R}\\ \frac{(A_2+2x_R)^2}{4A_2g_1(\beta)}-\frac{y_{R2}^2}{A_2g_2(\beta)}, & \text{if } -\pi+\arctan\frac{2y_{R2}}{A_2+2x_R}<\beta\leq-\pi+\arctan\frac{2B_2+2y_{R2}}{A_2+2x_R}\\ \frac{(B_2+y_{R2})^2}{A_2g_2(\beta)}-\frac{y_{R2}^2}{A_2g_2(\beta)}, & \text{if } -\pi+\arctan\frac{B_2+2y_{R2}}{A_2+2x_R}<\beta\leq-\arctan\frac{2B_2+2y_{R2}}{A_2-2x_R}\\ \frac{(A_2-2x_R)^2}{4A_2g_1(\beta)}-\frac{y_{R2}^2}{A_2g_2(\beta)}, & \text{if } -\arctan\frac{2B_2+2y_{R2}}{A_2-2x_R}<\beta\leq-\arctan\frac{2y_{R2}}{A_2-2x_R}\end{cases} \tag{A.32}$$

where $g_1(\beta)=2(B_1+B_2)\cos^2(\beta)$ and $g_2(\beta)=2(B_1+B_2)\sin^2(\beta)$.

THE FINAL EXPRESSIONS FOR THE PDFS OF THE TRANSMITTER AND THE RECEIVER DOPPLER FREQUENCIES

$$p_{\boldsymbol{f}_T}(f_T)=\begin{cases}
\frac{A_1}{D}\left[(G_{T2}^k)^2F_T-4y_{T2}^2f_T^2\right]f_{T_{\max}}^2, \\
\qquad \text{if } -\frac{G_{T2}^k f_{T_{\max}}}{\sqrt{(G_{T2}^k)^2+4y_{T2}^2}}<(-1)^k f_T\le -\frac{G_{T1}^k f_{T_{\max}}}{\sqrt{(G_{T1}^k)^2+4y_{T1}^2}}, k=0,1 \\
\frac{1}{D}\left[(A_2(G_{T1}^k)^2+A_1(G_{T2}^k)^2)F_T-4C_Tf_T^2\right]f_{T_{\max}}^2, \\
\qquad \text{if } -\frac{(G_{T1}^k) f_{T_{\max}}}{\sqrt{(G_{T1}^k)^2+4y_{T1}^2}}<(-1)^k f_T\le -\frac{(G_{T2}^k) f_{T_{\max}}}{\sqrt{(G_{T2}^k)^2+4E_{T2}^2}}, k=0,1 \\
\frac{1}{D}\left[(A_2F_T(G_{T1}^k)^2-4f_T^2(C_T-A_1E_{T2}^2)\right]f_{T_{\max}}^2, \\
\qquad \text{if} -\frac{G_{T2}^k f_{T_{\max}}}{\sqrt{(G_{T2}^k)^2+4E_{T2}^2}}<(-1)^k f_T\le -\frac{G_{T1}^k f_{T_{\max}}}{\sqrt{(G_{T1}^k)^2+4E_{T1}^2}}, k=0,1 \\
\frac{1}{F_T^{3/2}}\left[(A_2E_{T1}^2+A_1E_{T2}^2)-C_T\right]f_{T_{\max}}^2, \\
\qquad \text{if } -\frac{\left(\frac{A_1}{2}-x_T\right)f_{T_{\max}}}{\sqrt{\left(\frac{A_1}{2}-x_T\right)^2+E_{T1}^2}}<f_T\le\frac{\left(\frac{A_1}{2}+x_T\right)f_{T_{\max}}}{\sqrt{\left(\frac{A_1}{2}+x_T\right)^2+E_{T1}^2}},
\end{cases} \tag{A.33}$$

where $C_T=A_2y_{T1}^2+A_1y_{T2}^2$, $D=8A_1A_2(B_1+B_2)f_T^2(f_{T_{\max}}^2-f_T^2)^{3/2}$, $E_{T1}=B_1+y_{T1}$, $E_{T2}=B_2+y_{T2}$, $F_T=(f_{T_{\max}}^2-f_T^2)$, $G_{T1}^k=A_1-(-1)^k2x_T$, and $G_{T2}^k=A_2-(-1)^k2x_T$.

$$p_{\boldsymbol{f}_R}(f_R)=\begin{cases}
\frac{A_2}{D}\left[(G_{R1}^k)^2F_R-4y_{R1}^2f_R^2\right]f_{R_{\max}}^2, \\
\qquad \text{if } -\frac{G_{R1}^k f_{R_{\max}}}{\sqrt{(G_{R1}^k)^2+4y_{R1}^2}}<(-1)^k f_R\le -\frac{G_{R2}^k f_{R_{\max}}}{\sqrt{(G_{R2}^k)^2+4y_{R2}^2}}, k=0,1 \\
\frac{1}{D}\left[(A_2(G_{R1}^k)^2+A_1(G_{R2}^k)^2)F_R-4C_Rf_R^2\right]f_{R_{\max}}^2, \\
\qquad \text{if } -\frac{(G_{R2}^k) f_{R_{\max}}}{\sqrt{(G_{R2}^k)^2+4y_{R1}^2}}<(-1)^k f_R\le -\frac{G_{R1}^k f_{R_{\max}}}{\sqrt{(G_{R1}^k)^2+4E_{R1}^2}}, k=0,1 \\
\frac{1}{D}\left[4f_R^2(A_2E_{R1}^2-C_R)-A_1F_R(G_{R2}^k)^2\right]f_{R_{\max}}^2, \\
\qquad \text{if} -\frac{G_{R1}^k f_{R_{\max}}}{\sqrt{(G_{R1}^k)^2+E_{R1}^2}}<(-1)^k f_R\le -\frac{G_{R2}^k f_{R_{\max}}}{\sqrt{(G_{R2}^k)^2+4E_{R2}^2}}, k=0,1 \\
\frac{4f_R^2}{D}\left[(A_2E_{R1}^2+A_1E_{R2}^2)-C_R\right]f_{R_{\max}}^2, \\
\qquad \text{if } -\frac{\left(\frac{A_2}{2}-x_R\right)f_{R_{\max}}}{\sqrt{\left(\frac{A_1}{2}-x_R\right)^2+E_{R2}^2}}<f_R\le\frac{\left(\frac{A_2}{2}+x_R\right)f_{R_{\max}}}{\sqrt{\left(\frac{A_2}{2}+x_R\right)^2+E_{R2}^2}},
\end{cases} \tag{A.34}$$

where $C_R=A_2y_{R1}^2+A_1y_{R2}^2$, $D=8A_1A_2(B_1+B_2)f_R^2(f_{R_{\max}}^2-f_R^2)^{3/2}$, $E_{R1}=B_1+y_{R1}$, $E_{R2}=B_2+y_{R2}$, $F_R=(f_{R_{\max}}^2-f_R^2)$, $G_{R1}^k=A_1-(-1)^k2x_R$, and $G_{R2}^k=A_2-(-1)^k2x_R$.

REFERENCES

[1] F. Qu, F.-Y. Wang, and L. Yang, "Intelligent transportation spaces: vehicles, traffic, communications, and beyond," *IEEE Commun. Magazine*, vol. 48, no. 11, pp. 136–142, Nov. 2010.

[2] M. Pätzold and B. O. Hogstad, "A space-time channel simulator for MIMO channels based on the geometrical one-ring scattering model," in *Proc. 60th IEEE Semiannual Veh. Technol. Conf., VTC 2004-Fall. Los Angeles, CA, USA*, vol. 1, Sept. 2004, pp. 144–149.

[3] M. Pätzold, B. O. Hogstad, N. Youssef, and D. Kim, "A MIMO mobile-to-mobile channel model: Part I — the reference model," in *Proc. 16th IEEE Int. Symp. on Personal, Indoor and Mobile Radio Communications, PIMRC 2005. Berlin, Germany*, Sept. 2005, pp. 573–578.

[4] M. Pätzold and B. O. Hogstad, "A wideband MIMO channel model derived from the geometrical elliptical scattering model," *Wireless Communications and Mobile Computing*, vol. 8, pp. 597–605, May 2008.

[5] A. S. Akki and F. Haber, "A statistical model of mobile-to-mobile land communication channel," *IEEE Trans. Veh. Technol.*, vol. 35, no. 1, pp. 2–7, Feb. 1986.

[6] A. G. Zajić, G. L. Stüber, T. G. Pratt, and S. Nguyen, "Wideband mimo mobile-to-mobile channels: geometry-based statistical modeling with experimental verification," *IEEE Trans. Veh. Technol.*, vol. 58, no. 2, pp. 517–534, Feb. 2009.

[7] A. Chelli and M. Pätzold, "A MIMO mobile-to-mobile channel model derived from a geometric street scattering model," in *Proc. 4th IEEE International Symposium on Wireless Communication Systems, ISWCS 2007*. Trondheim, Norway, Oct. 2007, pp. 792–797.

[8] ——, "A non-stationary MIMO vehicle-to-vehicle channel model based on the geometrical T-junction model," in *Proc. International Conference on Wireless Communications and Signal Processing, WCSP 2009*. Nanjing, China, Nov. 2009.

[9] C. Wei, H. Zhiyi, X. Tao, and Z. Wei, "A novel isotropic scatter distribution wideband MIMO M2M fading channel model," in *Proc. 7th Annual Commu-*

nication Networks and Services Research Conference, CNSR'09., May 2009, pp. 443 –445.

[10] X. Cheng, C.-X. Wang, D. I. Laurenson, S. Salous, and A. V. Vasilakos, "An adaptive geometry-based stochastic model for non-isotropic MIMO mobile-to-mobile channels," *IEEE Trans. Wireless Commun.*, vol. 8, no. 9, pp. 4824–4835, Sep. 2009.

[11] I. Tan, T. Wanbin, K. Laberteaux, and A. Bahai, "Measurement and analysis of wireless channel impairments in DSRC vehicular communications," in *Proc. IEEE ICC'08*, May 2008, pp. 4882–4888.

[12] S. H. Kong, "TOA and AOD statistics for down link Gaussian scatterer distribution model," *IEEE Trans. Wireless Commun.*, vol. 8, no. 5, pp. 2609–2617, May 2009.

[13] Y. Ma and M. Pätzold, "Modelling and statistical characterization of wideband indoor radio propagation channels," in *Proc. International Congress on Ultra Modern Telecommunications and Control Systems and Workshops, ICUMT 2010*. Moscow, Russia, Oct. 2010, pp. 777–783.

[14] ——, "Design and simulation of narrowband indoor radio propagation channels under LOS and NLOS propagation conditions," in *Proc. IEEE 71st Vehicular Technology Conference, VTC2010-Spring*. Taipei, Taiwan, May 2010.

[15] M. Pätzold, *Mobile Fading Channels*. Chichester: John Wiley & Sons, 2002.

[16] A. Papoulis and S. U. Pillai, *Probability, Random Variables and Stochastic Processes*, 4th ed. New York: McGraw-Hill, 2002.